Scripta Materialia 279 (2026) 117308

Contents lists available at ScienceDirect

Scripta Materialia

journal homepage: www.journals.elsevier.com/scripta-materialia

Plastic yielding of mechanically confined submicron Li metal

Kunqing Ding [a], Tingting Yang [b], Hui Li [b], Congcong Du [b], Jun Zhao [b], Yin Zhang [c], Jianyu Huang [b,d,*], Ting Zhu [a,*]

[a] George W. Woodruff School of Mechanical Engineering, Georgia Institute of Technology, Atlanta, GA 30332, USA
[b] Clean Nano Energy Center, State Key Laboratory of Metastable Materials Science and Technology, Yanshan University, Qinhuangdao, Hebei 066004, China
[c] State Key Laboratory for Turbulence and Complex System, Department of Mechanics and Engineering Science, Peking University, Beijing 100871, China
[d] Hunan Provincial Key laboratory of Thin Film Materials and Devices, School of Materials Science and Engineering, Xiangtan University, Xiangtan, Hunan 411105, China

ARTICLE INFO

Keywords:
Li metal
Plastic yielding
All-solid-state batteries

ABSTRACT

Lithium (Li) metal is a leading anode candidate for high-performance all-solid-state batteries, yet its mechanical behavior at small length scales remains poorly understood. We employ an in situ environmental transmission electron microscopy–atomic force microscopy (ETEM–AFM) platform, combined with finite element modeling, to investigate the deformation behavior of submicron Li particles coated with a Li_2CO_3-rich solid electrolyte interphase (SEI) nanolayer. Under localized compression by the AFM tip, these particles experience highly heterogeneous multiaxial stress states and exhibit an effective yield strength of approximately 50 MPa. The low-crystallinity Li_2CO_3 shell deforms conformally with the Li core, accommodating large strains without fracture. These results reveal key mechanisms of plastic deformation in mechanically confined submicron Li and nanoscale Li_2CO_3, which are critical for enhancing the mechanical stability of Li anodes in all-solid-state batteries.

Introduction

The growing demand for electric vehicles and energy storage has intensified the need for durable, low-cost, and high-energy rechargeable batteries. Lithium (Li) metal is a leading candidate for anodes in all-solid-state batteries, due to its high energy density and low electrochemical potential [1,2]. However, progress in Li battery technology is hindered by uncontrollable dendritic or mossy Li growth [3–5], which can cause short circuits and premature failure of Li metal batteries (LMBs) [6–8]. Understanding the mechanical properties of Li at length scales and loading conditions relevant to LMB operation is critical to their development.

Recent studies have shown that the mechanical response of Li is strongly size-dependent. In bulk Li (grain size >10 μm) at room temperature, Tariq et al. [9] measured a Young's modulus of 7.8 GPa and a yield strength between 0.76 and 1.1 MPa, depending on loading rate. Lepage et al. [10] reported that Li exhibits noticeable strain hardening only at low temperatures (198 K), with negligible hardening at room temperature. Xu et al. [11] conducted in situ uniaxial compression tests on Li micropillars (1.17–8.49 μm in diameter) and observed a decrease in yield strength from 80 MPa to 18 MPa as pillar size increased. Fincher et al. [12] performed a systematic study from the nanoscale to bulk using nanoindentation and tensile testing, reporting yield strengths ranging from ~0.6 MPa in bulk to ~14 MPa at sub-10 μm scales, with strong rate sensitivity. Zhang et al. [13] measured compressive yield strengths as high as 244 MPa in submicron-diameter Li whiskers, demonstrating a clear "smaller-is-stronger" trend. The mechanical properties of Li are also known to be sensitive to impurity levels [14], which may contribute to the variation in reported yield strengths across different studies. While these studies provide valuable information on size-dependent yield strength under predominantly uniaxial loading, and some nanoindentation experiments also involve multiaxial stress states, the plastic yielding of small-scale Li under mechanical confinement by surrounding materials remains largely unexplored. Such conditions, however, are critical for understanding how Li deforms when confined by surrounding electrode and electrolyte materials in practical LMBs under stack pressure.

In addition, Li metal is typically covered by a thin solid electrolyte interphase (SEI) layer that plays a key role in battery performance [15–17]. Formed during initial lithiation, the SEI acts as a protective barrier that improves coulombic efficiency and limits further electrolyte decomposition, and it may also help suppress dendrite growth. Because

* Corresponding authors.
E-mail addresses: jhuang@ysu.edu (J. Huang), ting.zhu@me.gatech.edu (T. Zhu).

https://doi.org/10.1016/j.scriptamat.2026.117308
Received 19 January 2026; Received in revised form 11 March 2026; Accepted 27 March 2026
Available online 28 March 2026

the SEI is extremely thin and structurally complex, directly measuring its mechanical properties is highly challenging. Zhang et al. [13] estimated the Young's modulus of Li_2CO_3, a common SEI component, to be ~21.5 GPa using a rule-of-mixtures approach. Although progress has been made in synthesizing nanostructured, air-stable Li spheres, the mechanical properties of nanoscale SEI layers remain largely unknown.

In this work, we report compression experiments of individual submicron Li particles covered with a Li_2CO_3 nanolayer using an environmental transmission electron microscopy–atomic force microscopy (ETEM–AFM) platform. Force-displacement data from these experiments, combined with finite element method (FEM) modeling, enable extraction of the Young's moduli and effective yield strengths of both the Li core and the Li_2CO_3 shell. We show that the von Mises effective yield strength of submicron Li spheres reaches ~ 50 MPa, which is significantly higher than that of micron-sized Li particles. We further analyze the multiaxial stress states within the mechanically confined Li particles. These results offer mechanistic insight into the mechanical behavior of submicron Li and nanoscale Li_2CO_3 under complex multiaxial loading conditions, which is critical for the development of robust LMBs.

Experimental

Setup

In situ growth and compression experiments of Li particles were conducted using an ETEM–AFM platform. The operating principle of this platform has been described in detail in our previous work [13]. A

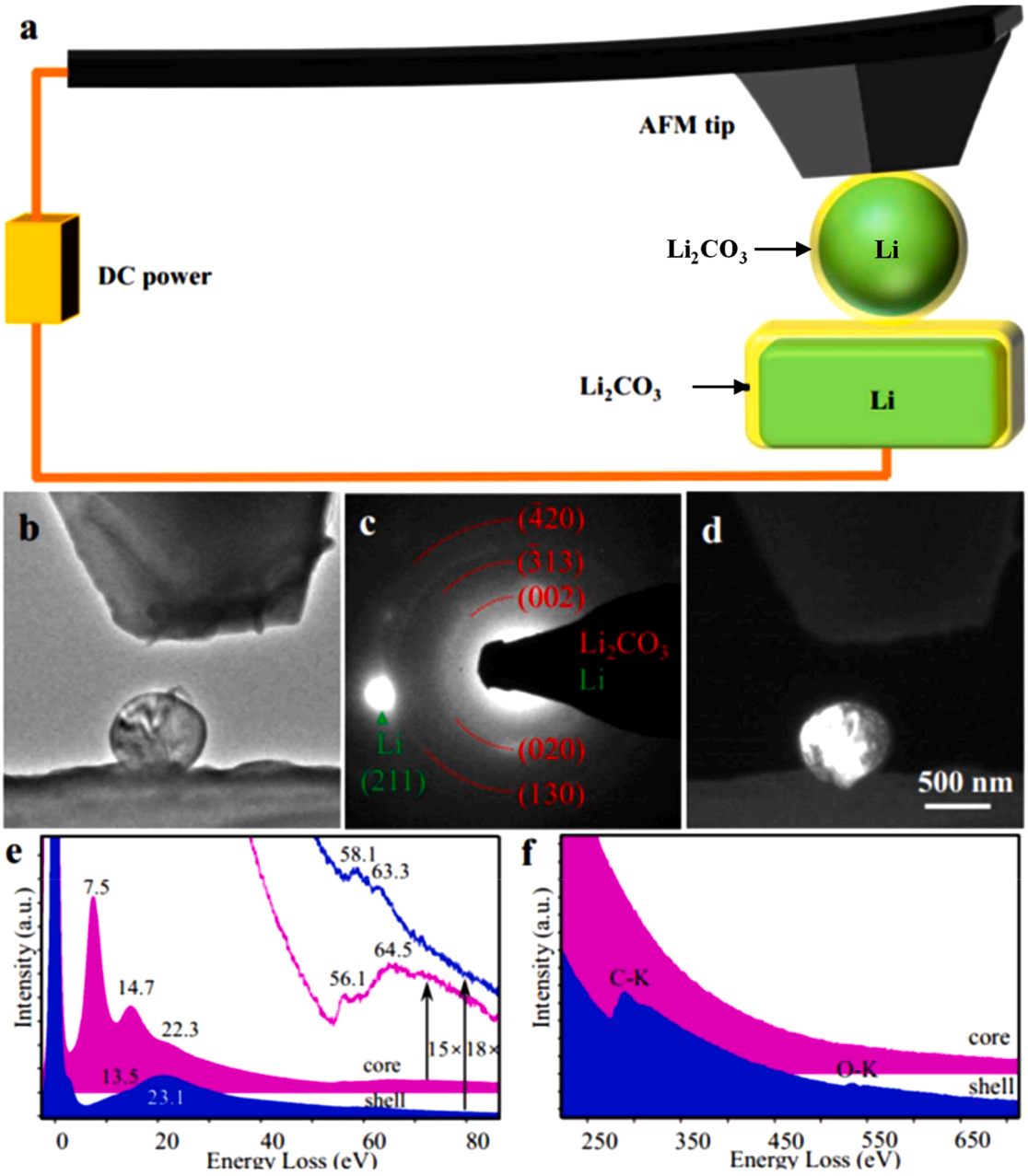

Fig. 1. In situ growth of a spherical Li particle and subsequent mechanical characterization. (a) Schematic illustration of the ETEM–AFM setup used for Li particle growth and mechanical testing. (b) Bright-field TEM image of a Li particle electrochemically grown beneath the AFM tip in a CO_2 atmosphere at 1 mbar. (c) Electron diffraction pattern (EDP) and (d) the corresponding dark-field TEM image of the same Li particle. (e) Low-loss and (f) core-loss electron energy loss spectroscopy (EELS) spectra of the Li particle, indicating the presence of a Li_2CO_3 shell on the particle surface.

schematic of the setup is shown in Fig. 1a. The electrochemical cell within the ETEM consists of a Li anode, a Li_2CO_3 solid electrolyte, and a silicon (Si)-based AFM cantilever serving as the counter electrode, forming a Li/Li_2CO_3/AFM(Si) configuration. This setup enables both in situ electrochemical growth of submicron Li particles and their subsequent mechanical testing.

During the experiment, an individual spherical high-purity Li particle was electrochemically grown beneath the AFM tip in a CO_2 atmosphere at 1 mbar pressure inside ETEM. After a submicron-sized particle formed, it was pushed upward by a piezo-controlled nanomanipulator connected to the underlying bulk Li source (Fig. 1a). As the particle moved upward, it deflected the AFM cantilever. The applied force (F) was determined from the AFM cantilever displacement (x), measured directly from TEM images, and the known cantilever spring constant (k), using Hooke's law, $F = k \cdot x$.

Results

Figures 1b–f show a Li particle grown in a CO_2 atmosphere, with a diameter of ~700 nm and a 30 nm-thick Li_2CO_3 surface layer. The core–shell structure is confirmed by the electron diffraction pattern (EDP, Fig. 1c) and electron energy loss spectroscopy (EELS, Fig. 1e and f). The EDP exhibits a single-crystal diffraction pattern from the Li core, indicating that the particle is a single crystal. The Li_2CO_3 shell exhibits diffuse diffraction rings, indicating low crystallinity. Notably, Li_2CO_3 is also a major component of the SEI in practical batteries. Therefore, characterizing the mechanical properties of these as-synthesized Li particles coated with a Li_2CO_3 shell is directly relevant to understanding and improving the performance of Li metal anodes.

Figure 2 presents sequential TEM images from an in situ compression test on a Li particle (~574.4 nm in diameter) with a Li_2CO_3 shell (~33.4 nm in thickness). Upon loading at a nominal strain rate of ~10^{-3} /s, defined as the indentation displacement rate normalized by the initial particle diameter, the particle underwent substantial deformation, characterized by pronounced vertical compression and lateral expansion. Owing to spherical geometry and localized AFM contact, the strain field within the particle is heterogeneous, and therefore the reported value represents a nominal deformation rate rather than a uniform strain rate. This deformation extended beyond the contact region and was distributed throughout the entire particle (Fig. 2a–i). During the test, the

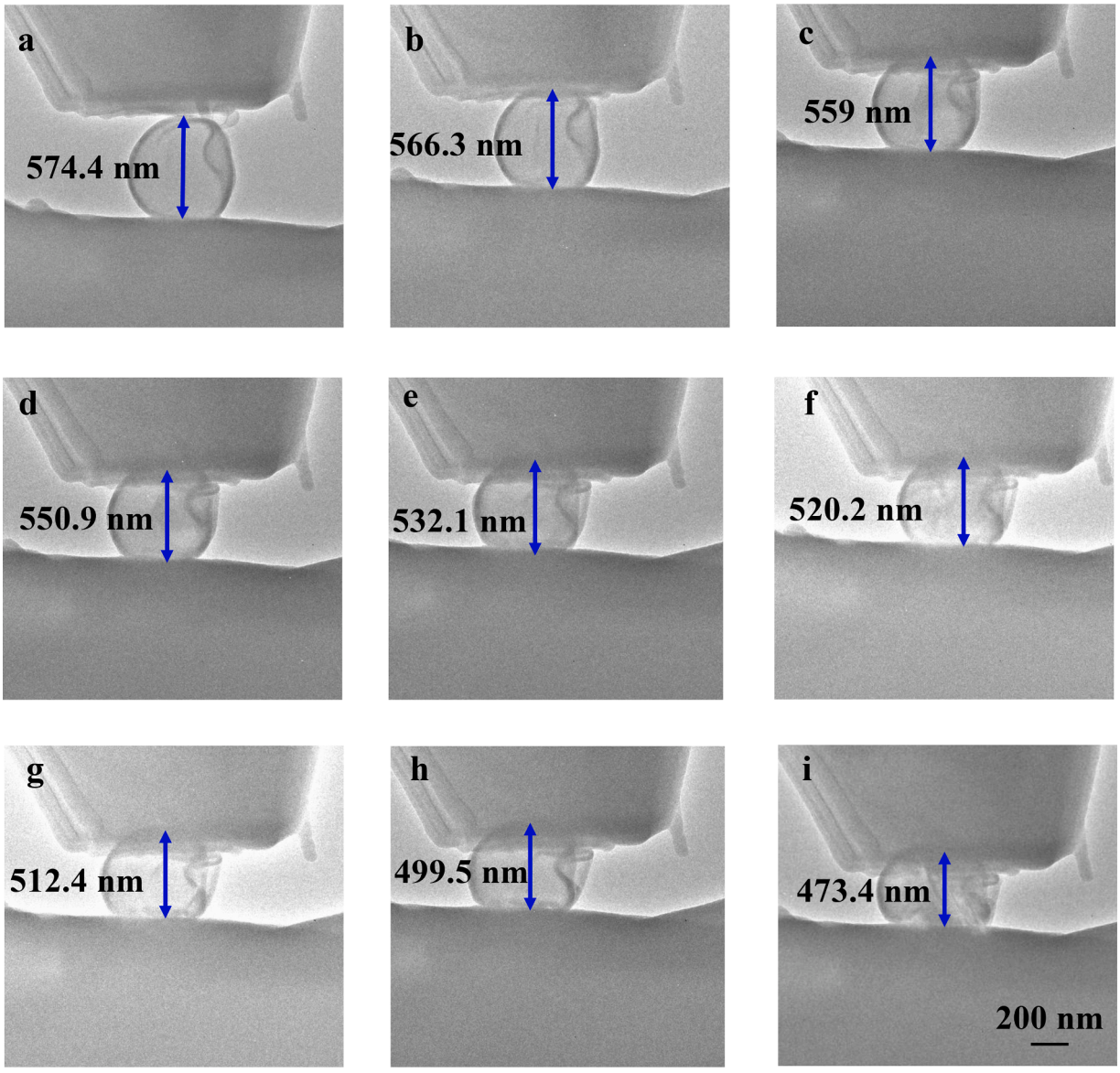

Fig. 2. In situ compression of a submicron Li particle coated with a Li_2CO_3 shell (a-i). Before compression, the particle has a height of ~574.4 nm and an average Li_2CO_3 shell thickness of ~33.4 nm (a). After compression, the particle height decreases to ~473.4 nm, corresponding to an overall compressive strain of ~16%.

Li_2CO_3 shell remained intact, showing no evidence of cracking or delamination. Instead, it deformed together with the Li core, conforming to the shape change from a particle to an oblate spheroid. Intimate core-shell contact was maintained even at compressive strains of ~16%. These observations indicate that the native Li_2CO_3 layer can withstand significant elastic and plastic strains without mechanical failure. This behavior is consistent with our previous observations that nanocrystalline or amorphous Li_2CO_3 exhibits considerable plasticity, with ultimate strengths ranging from 192 to 330 MPa [18]. These strength values are comparable to the compressive strength of Li dendrites [13], indicating the mechanical compatibility between the Li core and the Li_2CO_3 shell. Similar delocalized plastic deformation and intact interfaces were also observed in additional tests on a particle with a diameter of ~700 nm (Fig. A1).

Electron-beam-induced softening of lithium has been reported in previous TEM studies due to beam–matter interactions. The in situ mechanical testing was performed using the AFM–ETEM platform reported in our previous work on Li whiskers [13], where benchmark experiments comparing measurements from the AFM–ETEM system and a commercial TEM mechanical testing holder showed excellent agreement, confirming the reliability of the measurement system. In the present experiments, the electron beam intensity was minimized during mechanical testing to reduce potential beam effects. Moreover, the Li core is coated with a ~30 nm-thick Li_2CO_3 shell, which may partially attenuate direct beam–Li interactions. A rigorous beam-on/beam-off comparison is also experimentally challenging for the present system because electrochemically grown submicron Li particles may exhibit unavoidable variations in Li_2CO_3 shell thickness and local contact geometry near the AFM tip, both of which can influence the measured force–displacement response.

FEM modeling

Setup

To simulate the compression behavior observed in the in situ experiments, an axisymmetric finite element model was constructed using ABAQUS/CAE [19], as shown in Fig. 3. The model represents the core–shell particle shown in Fig. 2, which has a total diameter of 574.4 nm and consists of a Li core with a radius of 253.8 nm surrounded by a Li_2CO_3 shell with a thickness of 33.4 nm. Owing to axial symmetry, only one-quarter of the spherical particle was modeled. A tie constraint was imposed at the Li/Li_2CO_3 interface to ensure perfect bonding between the core and the shell. The AFM tip and the Li substrate were modeled as rigid bodies. Symmetry boundary conditions were applied along the central axis and the equatorial plane of the particle.

The contact geometry between the AFM tip and the particle was approximated based on TEM images obtained during and after compression. Specifically, the tip was represented by a spherical cap connected to a flat plate, which reflects the effective contact geometry observed in the experiments. The radius of the spherical cap and the vertical offset of the flat portion relative to the particle apex were measured directly from the TEM images and implemented in the FEM model. The Li core and the Li_2CO_3 shell were discretized using four-node axisymmetric solid elements (CAX4R). The Li core and Li_2CO_3 shell contain 2381 and 1050 elements, respectively.

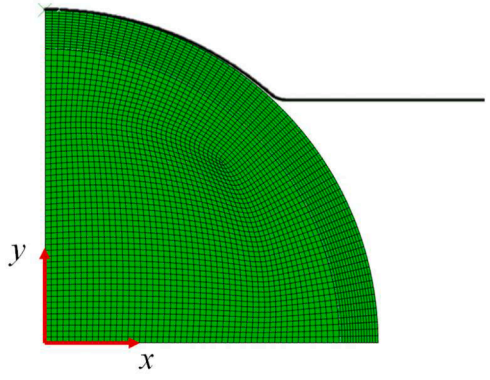

Fig. 3. FEM model of a core-shell particle in contact with an AFM tip, represented by a spherical cap connected with a flat plate (thick black line). Owing to axial symmetry, only one-quarter of the particle is modeled.

To capture the multiaxial stress states during compression, both Li and Li_2CO_3 were modeled using an isotropic J_2 plasticity formulation. Li was assumed to be perfectly plastic, consistent with previous experimental measurements showing negligible strain hardening at room temperature [10]. As a first-order approximation, the Li_2CO_3 shell was also modeled as perfectly plastic. A friction coefficient of 0.1 was used for the contact interaction between the AFM tip and the Li_2CO_3 shell. The elastic–plastic properties of the Li core and the Li_2CO_3 shell were calibrated through a parametric study in which the yield strength of Li, the yield strength of Li_2CO_3, and the Young's modulus of Li_2CO_3 were systematically varied. The best-fit parameters were obtained by simultaneously matching the experimentally measured force–displacement response and the lateral deformation of the particle during compression. Details of this parametric study are provided in the Supplementary Material (Fig. S1).

Results

Fig. 4a shows that the FEM-simulated force–displacement response of the AFM tip closely matches the experimental measurements. Similarly, Fig. 4b demonstrates good agreement between the FEM-simulated lateral strain–vertical strain response of the particle and the experimental data. The horizontal tensile strain was measured from the TEM images by tracking the lateral expansion of the particle boundary during compression and normalizing the particle diameter by its initial value. The best-fit mechanical properties are summarized in Table 1. For the core-shell particle with a total radius of 287.2 nm (Fig. 3), the extracted Young's modulus (E) and von Mises effective yield strength (σ_Y) of the Li core are ~11 GPa and ~55 MPa, respectively. This yield strength falls within the reported range for submicron-scale Li [13,18] and is substantially higher than those of micron-scale Li (>10 μm) [12,20] as discussed in the Introduction section, consistent with size-dependent strengthening. The extracted E and σ_Y of the Li_2CO_3 shell are ~27 GPa and ~37 MPa, respectively. While the Li_2CO_3 shell is elastically stiffer than the Li core, it is plastically softer. The mechanical effects of the Li_2CO_3 shell will be discussed in detail later. In addition, Fig. 4b shows that the lateral expansion of the Li particle is closely captured by the FEM simulation.

The robustness of these elastic–plastic properties is further supported by an independent compression experiment performed on another Li particle with a diameter of ~700 nm. The experimental observations and the corresponding FEM simulations for this particle are presented in the Supplementary Material (Figs. S2 and S3). The mechanical properties extracted from this additional test are consistent with those obtained from the particle shown in Fig. 2. In particular, the yield strength of the Li core obtained from the second particle (~49 MPa) is close to that obtained from the primary particle (~55 MPa), indicating good reproducibility of the measurements and the FEM calibration. The slightly lower yield strength measured for the larger particle may be attributed to the well-known size effect in small-scale Li, where smaller structures generally exhibit higher strength.

The experimental and simulation results (Fig. 4a) reveal a force-displacement response with two distinct compression stages, characterized by a steeper average slope in stage I than in stage II. To understand this behavior, we analyzed the distributions of von Mises effective stress (σ_e), axial stress (σ_{yy}), and hydrostatic pressure (P) at indentation depths (h) of 2 nm, 5 nm, 15 nm, and 60 nm measured relative to the Li

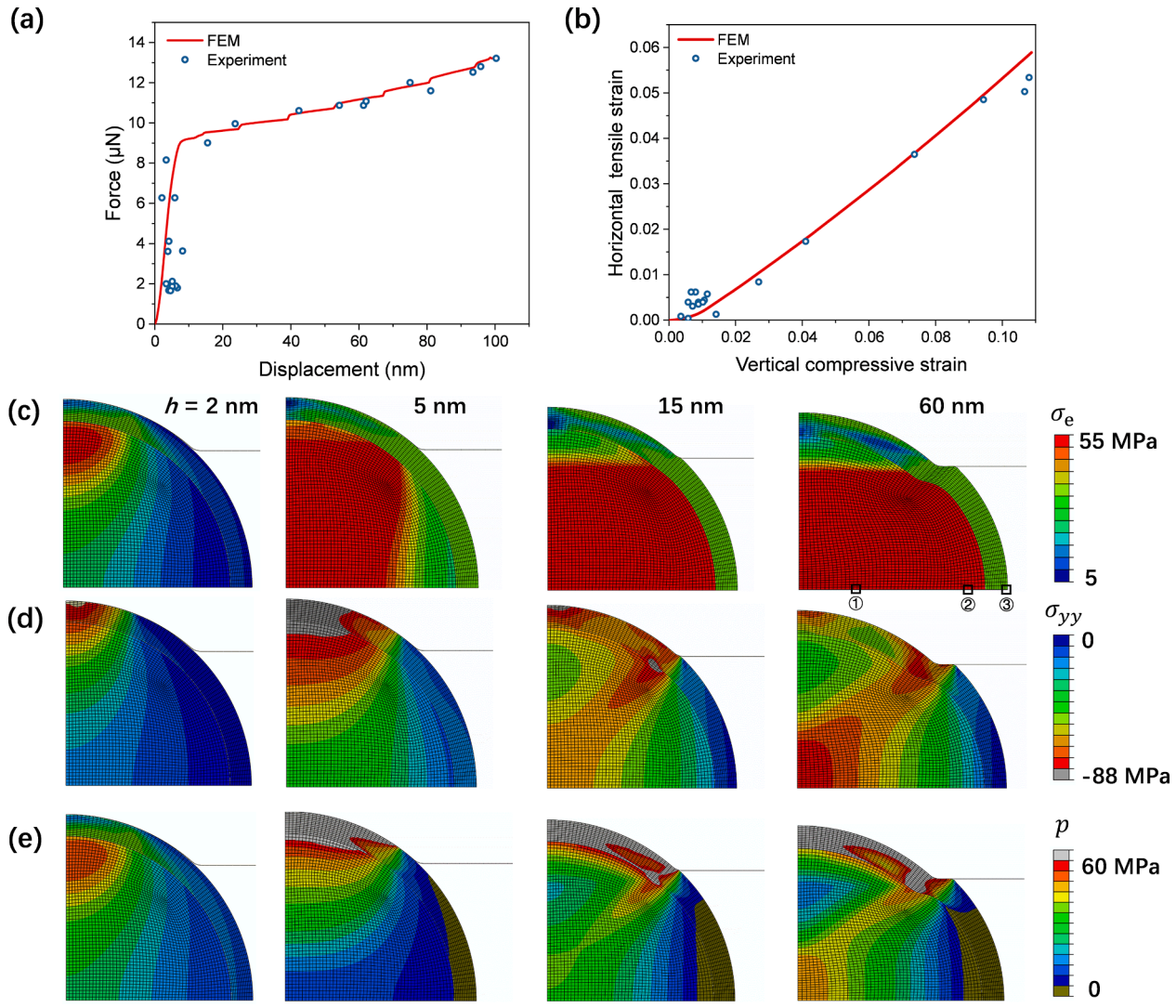

Fig. 4. Experimental and simulation results for compression of a core-shell particle with a total diameter of 574.4 nm, composed of a Li core with a radius of 253.8 nm and a surrounding Li_2CO_3 shell with a thickness of 33.4 nm. (a) Force-displacement response of the AFM tip from experimental measurements (circles) and FEM simulations (solid line). (b) Horizontal tensile strain versus vertical compressive strain from experimental measurements (circles) and FEM simulations (solid line). The vertical compressive strain is defined as the tip displacement normalized by the initial particle diameter, while the horizontal tensile strain is the lateral expansion normalized by the initial particle diameter. (c-e) FEM contour plots showing the distributions of (c) von Mises effective stress σ_e, (d) axial stress along the loading direction σ_{yy}, and (e) hydrostatic pressure P at the AFM tip displacement h of 2 nm, 5 nm, 15 nm and 60 nm measured relative to the Li metal substrate.

Table 1
Elastic-plastic properties of Li and Li_2CO_3 used in FEM simulations.

	E (GPa)	υ	σ_Y (MPa)
Li	11	0.3	55
Li_2CO_3	40	0.3	37

metal substrate (Fig. 4c–e). These stress fields capture the progression of plastic deformation in both the Li core and Li_2CO_3 shell. During the early part of stage I (e.g., h = 2 nm), the system remains largely elastic, resulting in a sharp increase in the AFM force. As compression proceeds in stage I (e.g., h = 5 nm), most of the Li particle reaches the von Mises effective yield strength σ_Y, indicating widespread plastic deformation. At this stage, high σ_{yy} and P are concentrated beneath the spherical cap of the AFM tip, where strong lateral confinement enhances resistance to deformation, giving rise to the steep slope observed in the force–displacement curve.

In stage II (e.g., h = 15 nm), the flat portion of the AFM tip comes into contact with the Li particle, leading to a pronounced reduction in the slope of the force–displacement curve. This softer response arises from two primary effects. First, the flat portion of the AFM tip provides less lateral confinement than the spherical cap, resulting in reduced σ_{yy} and P and a lower resistance to deformation. Second, a localized shear deformation zone begins to develop beneath the transition region between the spherical cap and flat portion of the tip, as indicated by elevated σ_{yy}. This shear zone, inclined at approximately 45° relative to the central axis, gradually extends toward the center of the Li particle. Owing to axial symmetry, this response corresponds to the formation of a conical shear zone within the three-dimensional Li particle. At larger compressions (e.g., h = 60 nm), the entire particle is displaced radially outward (rightward in the axisymmetric model), resulting in the characteristic elliptical shape of the compressed Li particle.

Multiaxial stresses

To understand the effects of mechanical confinement on stress distribution within the core-shell particle during compression, we analyzed the multiaxial stress states of three representative elements along the equatorial plane (as marked in Fig. 4c) at a compression displacement h

= 60 nm.

Element 1, located at the center of the Li core, experiences high compressive stresses: $\sigma_{xx} = -26.5$ MPa, $\sigma_{yy} = -77.3$ MPa, and $\sigma_{zz} = -18.9$ MPa. The corresponding hydrostatic pressure P, calculated as the negative average of the three normal stresses, is 40.9 MPa. The magnitude of σ_{yy} is much larger than that of σ_{xx}, and the difference between these stresses generates a large maximum shear stress, which drives local plastic yielding in this region.

Element 2, positioned near the Li/Li_2CO_3 interface but still within the particle, exhibits a markedly different stress state: $\sigma_{xx} = -7.4$ MPa, $\sigma_{yy} = -27.7$ MPa, and $\sigma_{zz} = 34.5$ MPa. The hydrostatic pressure here is only 0.2 MPa, much lower than that at the particle center due to its proximity to the particle surface. Compared to element 1, the reduced magnitude of σ_{yy} reflects reduced lateral constraint, while σ_{zz} becomes tensile, indicating the development of hoop tension caused by axial compression of the particle. In this region, plastic yielding is driven by the maximum shear stress arising from the difference between σ_{zz} and σ_{yy}.

Element 3, located on the outer free surface of the Li_2CO_3 shell, experiences $\sigma_{xx} = -0.1$ MPa, $\sigma_{yy} = -0.6$ MPa, and $\sigma_{zz} = 36.7$ MPa. Here, the axial stress σ_{yy} is negligible, and the mechanical responses are dominated by tensile hoop tension (σ_{zz}). Plastic yielding has also occurred in this surface region.

Overall, the above results reveal strongly heterogeneous multiaxial stress states across the particle. The hydrostatic pressure decreases from the particle interior toward the surface. Plastic yielding in the central core region is primarily driven by high compressive axial stress σ_{yy}, whereas near the surface, it is governed by significant hoop tension σ_{zz}. These findings highlight the highly inhomogeneous stress distribution that develops within the core-shell system under AFM compression.

Effects of the Li_2CO_3 shell

To further examine the effects of mechanical confinement provided by the Li_2CO_3 shell, we performed FEM simulations of a Li particle without the Li_2CO_3 shell (referred to as an all-Li particle) while maintaining the same total radius as the core-shell model. As shown in Fig. 5, the simulated load-displacement curve closely resembles that of the core-shell model in stage I, but shows an approximately 10% higher load in stage II. This modest increase in load-bearing capacity is attributed to the 33% higher yield strength of the Li compared to that of the Li_2CO_3 shell (Table 1).

In addition to differences in axial load response, the presence of the Li_2CO_3 shell significantly alters the stress distribution near the particle surface. For the all-Li particle, the stress state of the outermost element (corresponding to the location of Element 3 discussed in Section 3.3) is $\sigma_{xx} = -0.2$ MPa, $\sigma_{yy} = -3.7$ MPa, and $\sigma_{zz} = 56.6$ MPa. Notably, the magnitude of σ_{yy} is higher than that in the core-shell model. This difference arises from the mechanical confinement imposed by the Li_2CO_3 shell. Specifically, the elastically stiffer Li_2CO_3 shell imposes a stronger constraint on the lateral (x-direction) expansion of the Li core, generating additional internal pressure at the Li/Li_2CO_3 interface. This confinement induces an additional tensile stress component in the loading direction within the shell, thereby altering the local stress state.

Conclusions

We investigated the mechanically confined compressive deformation of individual submicron Li particles coated with a Li_2CO_3 nanolayer by combining in situ AFM-ETEM experiments with FEM modeling. The main findings and outlook are summarized below:

- *Integration of in situ experiments and modeling*: The combination of in situ AFM-ETEM experiments and FEM simulations provides direct and quantitative characterization of the elastic-plastic deformation of mechanically confined submicron Li and nanoscale Li_2CO_3 under complex multiaxial stress conditions. We determine a von Mises effective yield strength of ~55 MPa for submicron Li, which is consistent with previous reports from uniaxial tests at similar length scales but significantly higher than bulk Li (size > 10 μm).
- *Effects of multiaxial stresses and mechanical confinement*: FEM analysis of the core-shell structure under AFM compression reveals highly heterogeneous stress distributions within the Li particle due to localized AFM contact. Hydrostatic pressure peaks at the particle center and decreases toward the surface. Plastic yielding is primarily driven by high compressive axial stress in the central core region and by large hoop tension near the surface. Comparison with a homogeneous all-Li model shows that the Li_2CO_3 shell imposes only modest additional confinement. This behavior arises from the Li_2CO_3 shell's unique mechanical properties: although elastically stiffer than Li, the nanocrystalline/amorphous Li_2CO_3 layer is plastically softer, enabling conformal deformation with the highly ductile Li core.
- *Outlook*: This study provides critical mechanical benchmarks and mechanistic understanding of submicron Li and nanoscale Li_2CO_3 under non-uniform multiaxial stresses. These conditions are highly relevant to Li anode morphological evolution and dendrite growth in all-solid-state batteries during repeated cycling. Such spatially varying stress states are expected to profoundly influence electro-chemo-mechanical degradation pathways and long-term battery stability. Further systematic investigations are needed to quantitatively characterize these complex stress distributions, elucidate strain-rate effects, and assess their influence on Li plating/stripping kinetics and associated failure modes. Such efforts will pave the way

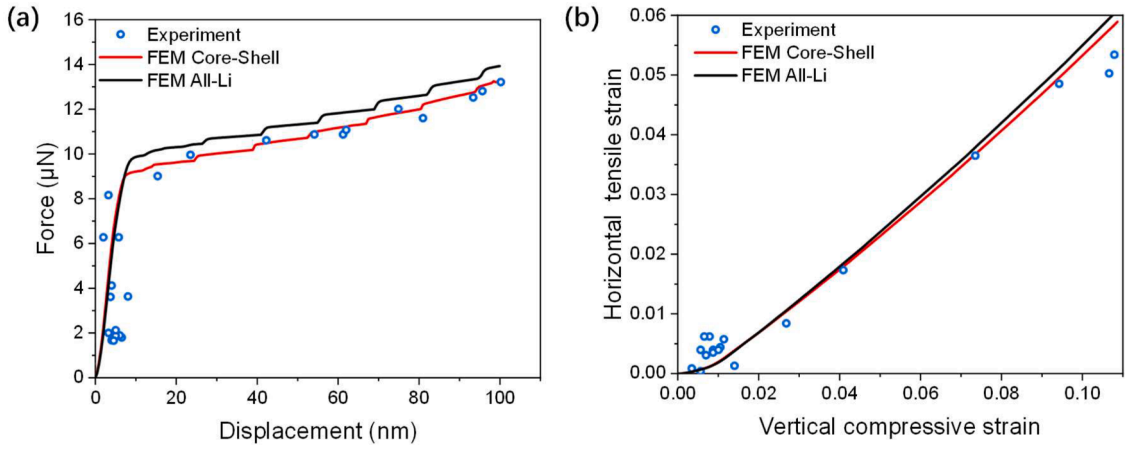

Fig. 5. Comparison of FEM-simulated results from the core-shell model (red line, Fig. 4) and the all-Li model (black line) along with experimental measurements (circles). (a) Force-displacement responses of the AFM tip. (b) Horizontal tensile strain versus vertical compressive strain.

for rationally designed, mechanically robust Li anodes in next-generation solid-state batteries.

CRediT authorship contribution statement

Kunqing Ding: Writing – original draft, Validation, Methodology, Investigation, Formal analysis, Data curation. **Tingting Yang:** Validation, Methodology, Investigation, Formal analysis, Data curation. **Hui Li:** Methodology, Investigation, Formal analysis, Data curation. **Congcong Du:** Methodology, Investigation, Formal analysis, Data curation. **Jun Zhao:** Methodology, Investigation, Formal analysis, Data curation. **Yin Zhang:** Methodology, Investigation, Formal analysis. **Jianyu Huang:** Writing – review & editing, Project administration, Methodology, Investigation, Formal analysis, Conceptualization. **Ting Zhu:** Writing – review & editing, Supervision, Project administration, Investigation, Conceptualization.

Declaration of competing interest

The authors declare that they have no known competing financial interests or personal relationships that could have appeared to influence the work reported in this paper.

Supplementary materials

Supplementary material associated with this article can be found, in the online version, at doi:10.1016/j.scriptamat.2026.117308.

References

[1] W. Xu, J. Wang, F. Ding, X. Chen, E. Nasybulin, Y. Zhang, J.-G. Zhang, Lithium metal anodes for rechargeable batteries, Energy Environ. Sci. 7 (2014) 513–537.
[2] S. Kalnaus, N.J. Dudney, A.S. Westover, E. Herbert, S. Hackney, Solid-state batteries: the critical role of mechanics, Science (1979) 381 (2023) eabg5998.
[3] J. Xiao, How lithium dendrites form in liquid batteries, Science (1979) 366 (2019) 426–427.
[4] A. Wang, S. Kadam, H. Li, S. Shi, Y. Qi, Review on modeling of the anode solid electrolyte interphase (SEI) for lithium-ion batteries, npj Comput. Mater. 4 (2018) 15.
[5] J. Steiger, D. Kramer, R. Mönig, Mechanisms of dendritic growth investigated by in situ light microscopy during electrodeposition and dissolution of lithium, J. Power Source. 261 (2014) 112–119.
[6] Y. Ren, Y. Shen, Y. Lin, C.-W. Nan, Direct observation of lithium dendrites inside garnet-type lithium-ion solid electrolyte, Electrochem. commun. 57 (2015) 27–30.
[7] Y. Suzuki, K. Kami, K. Watanabe, A. Watanabe, N. Saito, T. Ohnishi, K. Takada, R. Sudo, N. Imanishi, Transparent cubic garnet-type solid electrolyte of Al2O3-doped Li7La3Zr2O12, Solid. State Ion. 278 (2015) 172–176.
[8] E.J. Cheng, A. Sharafi, J. Sakamoto, Intergranular Li metal propagation through polycrystalline Li6.25Al0.25La3Zr2O12 ceramic electrolyte, Electrochim. Acta 223 (2017) 85–91.
[9] S. Tariq, K. Ammigan, P. Hurh, R. Schultz, P. Liu, J. Shang, Li material testing-fermilab antiproton source lithium collection lens, Proceedings of the 2003 particle accelerator conference, IEEE 3 (2003) 1452–1454, 1452-1454.
[10] W.S. LePage, Y. Chen, E. Kazyak, K.-H. Chen, A.J. Sanchez, A. Poli, E.M. Arruda, M. Thouless, N.P. Dasgupta, Lithium mechanics: roles of strain rate and temperature and implications for lithium metal batteries, J. Electrochem. Soc. 166 (2019) A89–A97.
[11] C. Xu, Z. Ahmad, A. Aryanfar, V. Viswanathan, J.R. Greer, Enhanced strength and temperature dependence of mechanical properties of Li at small scales and its implications for Li metal anodes, Proceed. Natl. Acad. Sci. 114 (2017) 57–61.
[12] C.D. Fincher, D. Ojeda, Y. Zhang, G.M. Pharr, M. Pharr, Mechanical properties of metallic lithium: from nano to bulk scales, Acta Mater. 186 (2020) 215–222.
[13] L. Zhang, T. Yang, C. Du, Q. Liu, Y. Tang, J. Zhao, B. Wang, T. Chen, Y. Sun, P. Jia, Lithium whisker growth and stress generation in an in situ atomic force microscope–environmental transmission electron microscope set-up, Nat. Nanotechnol. 15 (2020) 94–98.
[14] J. Aspinall, K. Sada, H. Guo, S. Kotakadi, S. Narayanan, Y. Chart, B. Jagger, E. Milan, L. Brassart, D. Armstrong, M. Pasta, The impact of magnesium content on lithium-magnesium alloy electrode performance with argyrodite solid electrolyte, Nat. Commun. 15 (2024) 4511.
[15] E. Peled, The electrochemical behavior of alkali and alkaline earth metals in nonaqueous battery systems—the solid electrolyte interphase model, J. Electrochem. Soc. 126 (1979) 2047.
[16] E. Peled, S. Menkin, SEI: past, present and future, J. Electrochem. Soc. 164 (2017) A1703.
[17] D. Aurbach, Review of selected electrode–solution interactions which determine the performance of Li and Li ion batteries, J. Power Source. 89 (2000) 206–218.
[18] H. Ye, S. Gui, Z. Wang, J. Chen, Q. Liu, X. Zhang, P. Jia, Y. Tang, T. Yang, C. Du, In situ measurements of the mechanical properties of electrochemically deposited Li2CO3 and Li2O nanorods, ACS Appl. Mater. Interface. 13 (2021) 44479–44487.
[19] ABAQUS/Standard 6.13, User's Manual, SIMULIA, Providence, RI, 2010.
[20] R.P. Schultz, Lithium: Measurement of Young's Modulus and Yield Strength, Fermi National Accelerator Lab., Batavia, IL (US), United States, 2002.